Research Square

Preprints are preliminary reports that have not undergone peer review.
They should not be considered conclusive, used to inform clinical practice,
or referenced by the media as validated information.

EGR1-AREG-EGFR Axis Drives Three-Dimensional Reprogramming of Intestinal Epithelium and Weaning-Induced Barrier Collapse: A Multi-Omics Causal Chain

Yu He

heyu@sxau.edu.cn

Shanxi Agricultural University

Dongjie Qu

Shanxi Agricultural University

Pan Liu

Shanxi Agricultural University

Wenpeng Yan

Shanxi Medical University

Ruirong Hao

Shanxi Agricultural University

Research Article

Keywords: Weaning stress, Enterocyte, EGR1, AREG-EGFR, Multi-omics, Intestinal barrier

Posted Date: August 25th, 2026

DOI: https://doi.org/10.21203/rs.3.rs-10752292/v1

License: This work is licensed under a Creative Commons Attribution 4.0 International License.
Read Full License

Additional Declarations: No competing interests reported.

Abstract

Background: Weaning stress disrupts the intestinal barrier in piglets, yet the cell-type-specific molecular programs remain unclear.

We re-analyzed public single-cell RNA sequencing data from GSE174112, covering 45,258 cells after quality control, and integrated temporal bulk RNA sequencing from PRJEB54752 with fecal metagenomics from PRJNA791695. Findings were validated in IPEC-J2 cells. Enterocytes emerged as the core responders. They expanded 2.4-fold in early-weaned piglets and carried 617 differentially expressed genes, which organized into a coordinated "stress–repair–immune attenuation" pattern with a stress–repair correlation of 0.78. The pattern combined marked oxidative stress, with MT3 at a $\log_2$FC of 10.92, autocrine repair activation, with AREG at 4.57, and innate immune attenuation. NicheNet and CellChat identified AREG-EGFR autocrine signaling as the dominant repair driver, Slingshot revealed premature repair activation at the transit-amplifying stage, and EGR1 was the most significantly upregulated transcription factor. WGCNA independently identified the weaning core module ME6, and metagenomics revealed pathogen enrichment together with butyrate-producer depletion. IPEC-J2 experiments confirmed the AREG-EGFR axis as the molecular switch for barrier imbalance.

Conclusions: Weaning stress thus disrupts the barrier through a "microbiota dysbiosis → butyrate depletion → EGR1 activation → AREG-EGFR repair → trajectory disorder" chain, highlighting the AREG-EGFR axis and butyrate supplementation as potential intervention targets.

Background

Weaning is the most critical stress transition in piglet production. Sow separation, abrupt diet conversion, and a new environment hit the piglet at the same time. Post-weaning diarrhea (PWD), reduced feed intake, and growth stagnation often follow, and the economic losses to the pig industry are substantial [1]. Enterocytes form the front line where the host meets luminal contents, and their barrier performance rests on tight junction proteins, antioxidant defense, and innate immune surveillance working together [2]. How weaning stress breaks this barrier at the level of individual cell types has remained poorly resolved.

Bulk transcriptome studies have long established oxidative stress, inflammation, and immune activation as hallmarks of weaning stress [3]. But bulk profiling averages the signal over all resident cell types. Contributions from individual populations can be masked, and opposite changes in two populations may even cancel out. Single-cell RNA sequencing (scRNA-seq) provides the resolution needed to separate these contributions.

Tang et al. [4] applied this approach to the ileum of weaned piglets. Their atlas (PRJNA728441; GSE174112) covers 42,149 cells and 24 subpopulations and documented marked remodeling of cellular composition and interaction networks after weaning. Wiarda et al. [5] profiled the porcine intestinal

lymphocyte compartment (GSE208613) and identified previously unrecognized innate lymphoid populations resembling their human counterparts. These atlases leave the enterocyte side of the story open. Which molecular programs do enterocytes engage under weaning stress? Which upstream regulators control them?

Repair of damaged intestinal epithelium depends heavily on the epidermal growth factor receptor (EGFR) pathway [6]. Among its ligands, amphiregulin (AREG) has attracted particular attention. Zaiss et al. [7] reviewed evidence that AREG acts in both immune regulation and tissue repair. Epithelial and immune cells alike can produce AREG, so the ligand can trigger EGFR through autocrine as well as paracrine routes to drive epithelial proliferation and barrier restoration. Which route operates during porcine weaning stress, and in which cell type the relevant signaling occurs, has not been determined.

Gut microbiota dysbiosis is another well-recognized companion of weaning stress [2, 8]. During this period the piglet gut community passes through a dramatic succession: beneficial bacteria decline while potential pathogens expand [2]. Much of the barrier-protective effect of the microbiota has been attributed to butyrate, the principal microbial short-chain fatty acid (SCFA). Butyrate fuels colonic epithelial cells. Through histone deacetylase (HDAC) inhibition and GPR43 activation, it also raises tight junction protein expression [2]. The mechanism has strong experimental support. Wang et al. [9] reported that butyrate upregulates claudin-1 transcription. Liu et al. [10] showed that sodium butyrate supplementation in weaned piglets increased beneficial bacteria, raised occludin and ZO-1 expression, and lowered intestinal permeability. Zheng et al. [11] demonstrated that microbiota-derived butyrate reinforces the barrier through IL-10 receptor-dependent repression of claudin-2.

These studies have revealed the pathology of weaning stress from three angles: cellular heterogeneity, signaling pathways, and microbiota metabolism. Systematic integration of the three dimensions is still lacking, and several questions remain open. What are the cell-type-specific response programs of enterocytes? Which transcriptional regulators sit upstream? How much do autocrine and paracrine signals each contribute? And how does microbiota dysbiosis drive epithelial dysfunction? In this study, we re-analyzed public scRNA-seq data and integrated temporal bulk RNA-seq with metagenomic data, moving stepwise from cellular composition to molecular programs, regulatory networks, dynamic processes, and microbiota tracing. Our aim was to construct a complete cross-omics mechanistic chain of weaning stress-induced intestinal barrier imbalance and to provide targets for precise intervention against PWD.

Methods

Data sources and preprocessing

The three public datasets integrated here came from independent published studies. All of them, however, used a 28-day-old weaned piglet model and therefore share a common biological background.

Single-cell RNA sequencing. Single-cell data were obtained from the public dataset GSE174112 [4], which contains ileal single-cell transcriptomes from 28-day-old piglets. The dataset holds 6 samples, three normal suckling piglets (NSP1, NSP2, NSP3) and three early-weaned piglets (EWP1, EWP2, EWP3). We retained all 6 samples because sample quality and group balance were both satisfactory. Reads were aligned to the porcine reference genome Sscrofa11.1 (Ensembl v100 annotation) with Cell Ranger v7.0.0. Quality control kept cells with more than 200 expressed genes and below the 99th percentile. Porcine mitochondrial genes lack the human-style MT- prefix, so conventional MT% filtering could not be computed reliably and was not applied.

SoupX v1.5.2 estimated and removed ambient RNA contamination, and Scrublet v0.2 excluded cells with doublet probability above 0.25. Batch correction used Harmony [12] through the IntegrateLayers method in Seurat v5. The first 30 principal components entered PCA, UMAP visualization used min.dist of 0.3 and n.neighbors of 30, and unbiased clustering ran at a resolution of 0.8 in Seurat v5 [13]. Residual batch effects remained after correction, with EWP3 dominating parts of the UMAP. Differential testing was therefore run at the single-cell level as described below, so that expression information from every cell was used.

Bulk RNA-seq. Temporal bulk RNA-seq data came from the European Nucleotide Archive (PRJEB54752 [14]). The 24 samples cover days 1, 4, and 14 after weaning, together with unweaned controls. Salmon v1.10.0 performed quasi-mapping and quantification against the Sscrofa11.1 reference transcriptome, tximport v1.26.0 summarized counts to the Gene Symbol level, and DESeq2 v1.38.0 was used for normalization.

Metagenomics. Fecal metagenomic data were downloaded from NCBI SRA (PRJNA791695 [15], 24 samples). Reads passed quality control with Trimmomatic v0.39, species annotation used Kraken2 v2.1.2 with the minikraken2_v8GB database, and Bracken v2.7 re-estimated abundance.

Single-cell analysis

Normalization and clustering were performed in Seurat v5. Preliminary differential expression screening used Wilcoxon rank-sum tests with Bonferroni correction, $|\log_2 FC|$ above 0.25, and min.pct above 0.25. Core DEGs had to pass the strict threshold of $|\log_2 FC|$ above 1 and corrected p below 0.05 before entering enrichment analysis.

Cell-type annotation rested on five layers of evidence. First, marker gene expression from FindAllMarkers with min.pct of 0.25 and logfc.threshold of 0.25. Second, the top marker heatmap, which validated cluster-specific expression patterns (Figure S4). Third, cell-cycle scoring confirmed the identity of proliferating and TA cells. Fourth, per-cluster sample-source stacked plots excluded batch-dominant effects (Fig. 1G). Fifth, per-sample cell-composition stacked plots verified intra-group reproducibility (Figure S5).

We constructed a three-dimensional scoring system. The stress score combined MT3, MT1A, and MT2A, the repair score combined AREG, HBEGF, EREG, CLDN4, TNFAIP3, and CCL20, and the immune attenuation score combined SFTPD, LBP, IFITM3, ISG15, and IFIT5. Scores were calculated with AddModuleScore on the basis of these literature-curated gene sets, and CellCycleScoring removed cell-cycle effects.

Cell interaction and trajectory analysis

NicheNet analysis. NicheNet v1.1.0 [16] calculated Spearman correlation coefficients between immune ligands and enterocyte target genes, using ligand-receptor databases together with the differentially expressed genes. This evaluated the regulatory potential of each ligand on target gene expression programs.

CellChat analysis. CellChat v1.6.0 [17] inferred cell-cell communication networks from ligand-receptor databases. Communication probabilities were calculated and then compared between the EWP and NSP groups.

Slingshot pseudotime analysis. Slingshot v2.4.0 [18] constructed epithelial differentiation trajectories on UMAP coordinates. Proliferating epithelium served as the starting point (start.clus = "Proliferating_Epithelial"), transit-amplifying (TA) cells as the intermediate state, and enterocytes and goblet cells as the terminal endpoints. Gene dynamics were analyzed along Lineage 1 pseudotime, and loess locally weighted regression smoothed the expression trends.

WGCNA analysis

WGCNA analysis. WGCNA v1.72-1 [19] ran blockwise module detection on 15,000 highly variable genes from the 24 bulk samples. The pickSoftThreshold function selected the soft-thresholding power, and power 6 gave a scale-free topology fitting index R^2 of 0.747 with mean connectivity below 100, close to the conventional threshold for biological network analysis. We constructed a signed hybrid TOM similarity matrix. Dynamic tree cutting with minModuleSize of 30 and deepSplit of 2 produced the initial modules, and modules whose eigengenes correlated above 0.75 were merged at mergeCutHeight of 0.25. Pearson correlations were calculated between module eigengenes (MEs) and traits, namely weaning status, time, and sex. Hypergeometric tests (phyper) assessed the significance of overlap between modules and single-cell enterocyte DEGs against the background of the 15,000 WGCNA input genes.

Mfuzz temporal clustering. Mfuzz v2.60.0 [20] performed fuzzy c-means clustering on ME6 module genes, with c of 6, m of 1.25, and a membership cutoff of 0.5.

Metagenomic analysis

Kraken2 species-level read counts formed an abundance matrix. Unclassified reads were removed, and counts were converted to relative abundance. The vegan package (v2.6-4) provided alpha diversity indices (Shannon and Simpson) and beta diversity based on Bray-Curtis distance. PCoA used the Bray-Curtis distance matrix, and PERMANOVA (adonis2, 999 permutations) tested between-group differences. Differential species were called by Wilcoxon rank-sum tests with BH correction at FDR below 0.05, and $\log_2$FC was calculated from CLR-transformed abundance.

Cell-based validation of the AREG-EGFR axis

IPEC-J2 cells, a porcine small intestinal epithelial cell line (ATCC CRL-183), were cultured in DMEM/F12 with 10% FBS and 1% penicillin-streptomycin at 37°C and 5% CO_2. Cells reaching 80%–90% confluence were serum-starved for 12 h and assigned to six groups: Control; TNF-α at 10 ng/mL; IFN-γ at 10 ng/mL; TNF + IFN at 10 + 10 ng/mL to mimic the weaning inflammatory microenvironment; TNF + IFN plus 10 μM gefitinib, an EGFR inhibitor; and TNF + IFN plus 100 ng/mL recombinant AREG (rAREG). The 24 h time point served as the main detection point.

qPCR. MT3, AREG, CLDN4, SFTPD, and IFITM3 expression was measured with GAPDH as the reference gene and the $2^{-}\Delta\Delta Ct$ method.

Western blot. EGFR, p-EGFR (Tyr1068), MT3, and CLDN4 protein levels were detected with primary antibodies at 1:1,000, secondary antibodies at 1:5,000, and ECL development.

ELISA. Porcine AREG and CCL20 quantitative kits measured secreted protein concentrations in the culture medium.

Barrier function detection. Transepithelial electrical resistance (TEER) was measured with a Millicell ERS-2 system. Paracellular permeability was assessed with 4 kDa FITC-dextran at 1 mg/mL on a fluorometer at 490/520 nm excitation/emission.

Rescue experiment. Gefitinib or rAREG was added to the respective groups after 12 h of TNF + IFN treatment, and incubation continued for another 12 h before the indicators above were detected.

Results

Weaning stress reshapes ileal cellular composition

The six 28-day-old piglets, three early-weaned (EWP1, EWP2, EWP3) and three normal suckling (NSP1, NSP2, NSP3), yielded 48,348 raw cells. Quality control retained cells with nFeature_RNA above 200 and below the 99th percentile, leaving 45,258 cells, with per-sample yields between 6,705 and 10,026 cells (Figure S1). Post-QC distributions of nCount_RNA and nFeature_RNA were balanced across samples, with no outliers (Figure S2).

Unbiased clustering in Seurat v5 identified 27 cell clusters, integrated into 25 reproducible clusters after Harmony batch correction (Fig. 1A–C). Before correction, UMAP plots colored by sample showed clear batch separation among the 6 samples. Mixing improved after correction, although EWP3 still dominated some regions, pointing to residual batch effects (Figure S3). Differential testing therefore ran at the single-cell level with Wilcoxon rank-sum tests, retaining expression information from every cell.

Cluster identities were assigned by weighing three lines of evidence together: marker gene expression, the top marker heatmap (Figure S4), and cell-cycle scoring. This resolved the clusters into 14 cell types. Proliferating/TA epithelial cells comprised clusters 0, 1, 2, 5, 6, 9, 13, and 14, cluster 10 corresponded to absorptive enterocytes, cluster 20 to secretory enterocytes, and cluster 26 to goblet cells. The immune compartment included B cells (cluster 4), $CD4^+$ T cells (cluster 12), cytotoxic T lymphocytes (cluster 17), NK cells (cluster 21), myeloid cells (clusters 19, 22, and 24), plasma cells (clusters 7 and 8), and innate lymphoid cells (cluster 23). Fibroblasts formed cluster 25, general epithelial/transitional cells clusters 3 and 15, and a high-mitochondrial population cluster 16 (Fig. 1D).

To validate annotation accuracy, we performed three supplementary analyses. First, per-cluster sample-source stacked bar plots showed that nearly all clusters were evenly represented across the 6 samples. Only cluster 16, the high-mitochondrial population, showed slight EWP3 dominance, confirming its batch-specific nature (Fig. 1G). Second, Top 5 marker DotPlots displayed the signature genes of each cluster, such as FABP2 and VIL1 for cluster 10 absorptive enterocytes, GUCA2A and CEACAM20 for cluster 20 secretory enterocytes, CD4 and PDCD1 for cluster 12 $CD4^+$ T cells, and CD8A and GZMK for cluster 17 CTLs, supporting annotation reliability (Fig. 1H).

Finally, cell-cycle scoring placed the proliferating/TA clusters predominantly in S or G2M phase, whereas terminally differentiated cells told the opposite story, with 95.8% of cluster 10 enterocytes and 88.2% of cluster 26 goblet cells in G1. These patterns fully match the proliferating/TA annotations (Fig. 1I). Per-sample cell-composition stacked plots showed good intra-group reproducibility, and NSP versus EWP differences lay mainly in immune cell proportions and epithelial differentiation states (Figure S5).

Cell-composition analysis revealed significant remodeling between NSP and EWP. Enterocytes, combining clusters 10 and 20, expanded 2.4-fold in EWP, from 2.4% to 5.8% of all cells (Fisher's exact test, $p = 3.69\times10^{-75}$), whereas proliferating/TA epithelial cells contracted, with an OR of 0.75 and $p = 2.8\times10^{-23}$ for cluster 0. Immune cells infiltrated significantly. CTLs (cluster 17) showed the most dramatic increase, with an OR of 4.96 at $p = 1.4\times10^{-73}$, followed by NK cells (cluster 21, OR 1.81), myeloid cells (cluster 19, OR 1.91), $CD4^+$ T cells (cluster 12, OR 1.47), and γδ T/NKT cells (cluster 15, OR 1.49), each significant at $p \le 8.3\times10^{-6}$. B cells moved the other way, with an OR of 0.88 and $p = 2.78\times10^{-12}$ for cluster 4, and TA epithelial cells (clusters 0, 2, and 5) all had ORs below 1. Goblet cells also increased significantly in EWP, with an OR of 4.46 and $p = 1.9\times10^{-7}$ for cluster 26, and plasma cells (clusters 7 and 8) together with fibroblasts (cluster 25) trended upward (Fig. 1E–F). Weaning stress therefore induces coordinated changes in the epithelial and immune compartments.

Enterocytes are the core responder cells to weaning stress

Combining the absorptive cluster 10 and the secretory cluster 20, enterocytes carried 617 differentially expressed genes in EWP versus NSP, with 472 upregulated and 145 downregulated at $|\log_2 FC|$ above 0.25 by Wilcoxon rank-sum test with Bonferroni correction and min.pct above 0.25. No other epithelial subpopulation came close (Fig. 2A–B). The proportional increase of enterocytes was also statistically significant (Fig. 2C). At the strict threshold of $|\log_2 FC|$ above 1 and corrected p below 0.05, 245 core DEGs remained: 174 upregulated and 71 downregulated (Figure S6).

The top 10 upregulated genes were MT3 at a $\log_2 FC$ of 10.92, ENSSSCG00000023305 at 8.95, ENSSSCG00000032591 at 6.76, MT1A at 6.70, ENSSSCG00000024911 at 6.10, MT2A at 5.00, EDN1 at 4.85, CCL20 at 4.62, AREG at 4.57, and HBEGF at 4.14. This profile indicates severe oxidative stress together with autocrine repair activation. Among the downregulated genes, PROS1 fell by 3.67 $\log_2$ units, SFTPD by 3.31, and LBP by 3.02, pointing to attenuated innate immune defense and barrier maintenance (Fig. 2D–F).

GO enrichment told two opposite stories. Upregulated genes at the standard threshold mapped to 51 significant BP terms, and the number rose to 110 at the strict threshold (Fig. 2G). Strongly differential genes are thus more concentrated in energy metabolism and stress response, whereas weakly differential genes add noise that dilutes enrichment. Downregulated genes showed the reverse: 27 significant terms at the standard threshold collapsed to only 2 at the strict threshold, indicating high functional heterogeneity and the simultaneous silencing of multiple immune and metabolic pathways (Fig. 2H). KEGG analysis identified 20 significant pathways at the standard threshold. The top-ranked terms were cell adhesion & migration, innate immune defense, inflammatory & immune signaling, ER stress & apoptosis, and prion disease; metabolic pathways such as carbon metabolism, oxidative phosphorylation, steroid biosynthesis, and the citrate cycle (TCA cycle) were also significantly enriched (Fig. 2I). GSEA added 41 significant pathways, and the oxidative stress, inflammatory response, and TNF signaling gene sets showed marked positive enrichment (Fig. 2J).

Enterocytes exhibit a three-dimensional stress–repair–immune attenuation pattern

To quantify enterocyte phenotypes systematically, we built a three-dimensional scoring system from curated gene sets drawn from the top DEGs: an antioxidant stress score built on MT3, MT1A, and MT2A, an autocrine repair score built on AREG, HBEGF, EREG, CLDN4, TNFAIP3, and CCL20, and an innate immune attenuation score built on SFTPD, LBP, IFITM3, ISG15, and IFIT5 (Fig. 3A). All three indices differed significantly between groups. The stress score rose from a mean of − 1.22 in NSP to 0.31 in EWP, and the repair score rose from − 0.32 to 0.10, both at Wilcoxon $p < 2.2\times10^{-16}$, while the immune attenuation score fell from 0 to − 0.14 at $p = 1.18\times10^{-13}$ (Fig. 3B–D). On the three-dimensional scatter plot, EWP enterocytes occupied a unique phenotypic space of high stress, high repair, and low immunity (Fig. 3E). Single-gene validation confirmed the score distributions (Fig. 3F–G; Figure S8). Stress and repair scores were strongly correlated, with a Pearson r of 0.78 at $p < 2.2\times10^{-16}$, indicating coordinated activation of defense and repair (Fig. 3H).

Immune-enterocyte interaction and autocrine AREG-EGFR signaling

The immune infiltration seen in Fig. 1 raised a question: do immune-derived signals drive the enterocyte alterations? We used NicheNet to associate immune-cell-derived ligands with enterocyte target genes, and the analysis returned 27 significant ligand–target pairs at $p < 0.05$ and $|r|$ above 0.1 (Figure S9). AREG showed the strongest positive regulatory potential for repair and stress targets, with r reaching 0.36 for EREG, 0.29 for MT3, and 0.27 for CCL20. The TGFA–EREG correlation reached 0.20 at $p = 2.31\times10^{-291}$. Immune-derived paracrine signals, by contrast, showed lower predicted association strength than the AREG autocrine loop (Fig. 4A–D). AREG produced by enterocytes themselves therefore appears to be the primary driver of the repair program.

CellChat network analysis confirmed this picture. AREG-EGFR communication strength rose by 38% in EWP compared with NSP (Fig. 4G–H; Figure S10). Sender-cell ligand dot plots covering myeloid cells, NK cells, CTLs, $CD4^+$ T cells, and fibroblasts showed elevated TNF, IFNG, IL6, OSM, EGF, TGFA, and AREG expression in EWP (Fig. 4E). IL1B went undetected in sender-cell transcriptomes, plausibly because myeloid cells are lost during tissue dissociation. On the receptor side, enterocytes expressed EGFR together with ERBB2, ERBB3, IGF1R, MET, and OSMR (Fig. 4F). Among key ligand–receptor pairs, AREG-EGFR was the most consistently enhanced interaction in EWP (Fig. 4H). Enterocyte repair is therefore driven mainly by autocrine AREG-EGFR signaling rather than paracrine immune signals.

Repair program is prematurely activated along the differentiation trajectory

To determine when the stress-repair program switches on during differentiation, we ran Slingshot trajectory analysis on the epithelial subset of 16,190 cells. The trajectory started from proliferating epithelium, passed through TA cells, and ended at enterocytes and goblet cells (Fig. 5A–B; Figure S11). In EWP, stress-repair genes such as MT3, MT1A, AREG, CLDN4, and CCL20 were already highly expressed at early differentiation stages, and high expression persisted through terminal differentiation. In NSP, the same genes peaked only at the terminal enterocyte stage (Fig. 5C). Proliferation markers BARD1, MCM7, and TYMS declined earlier in EWP, and the immune gene SFTPD stayed suppressed along the whole trajectory (Fig. 5D).

Pseudotime ranged from 0 to 16.76 on the raw scale. EWP and NSP distributions differed significantly, with a Kolmogorov–Smirnov D of 0.068 at $p = 3\times10^{-14}$, and the EWP median of 8.72 sat below the NSP median of 8.82. EWP cells therefore skew toward earlier differentiation stages (Fig. 5E). Within the enterocyte subset of 3,378 cells, the stress score correlated strongly with pseudotime in EWP, with a Spearman r of 0.75 at $p < 2.2\times10^{-16}$; the correlation in NSP was weaker but still significant, at r of 0.62 and $p = 1.4\times10^{-85}$ (Fig. 5F; Figure S12). The stress-repair program is thus prematurely activated during differentiation, which implies a dysregulated differentiation trajectory under weaning stress.

EGR1 transcriptional regulation and regulatory network

To find the upstream regulators, we examined candidate transcription factors (TFs) known to control core response genes. EGR1 was the most significantly upregulated TF in EWP enterocytes, with a median expression of 1.701 versus 0 in NSP (Wilcoxon $p < 2.2\times10^{-16}$), followed by NFE2L2 and MTF1 (Fig. 6A–B). EGR1 belongs to the C2H2-type zinc-finger family of transcription factors [21]. Oxidative stress and inflammatory stimuli can induce it rapidly, and it regulates downstream targets by binding GC-rich promoter elements. Every literature-reported EGR1 target we examined, including MT3, MT1A, AREG, HBEGF, EREG, CCL20, TNFAIP3, and CLDN4, was upregulated in EWP (Fig. 6C; Figure S13).

Cell-level Spearman correlation confirmed the relationship. EGR1 correlated positively with CLDN4 at r of 0.49, TNFAIP3 at 0.48, CCL20 at 0.46, EREG at 0.45, AREG at 0.32, HBEGF at 0.26, MT1A at 0.25, and MT3 at 0.18 (Fig. 6D). A regulatory network built from significant NicheNet correlations at $p < 0.01$ and $|r|$ above 0.15 contained 11 nodes and 14 edges, and AREG was the core node, with the highest degree centrality of 10 (Fig. 6E–F). These findings integrate into a dual-track model: immune infiltration activates EGR1, which then drives antioxidant defense through MT3 and MT1A via MTF1 and NFE2L2, plus autocrine repair through AREG, HBEGF, and EREG via EGFR (Fig. 6G).

WGCNA temporal validation

To validate the temporal dynamics of the enterocyte response, we performed weighted gene co-expression network analysis (WGCNA) on bulk RNA-seq data from 24 piglets in PRJEB54752 [14], sampled on days 1, 4, and 14 after weaning together with unweaned controls. With the soft-thresholding power set to 6, giving R^2 of 0.747, the analysis resolved 16 co-expression modules (Fig. 7A–C; Figure S14–S16). Module ME6 correlated most strongly with weaning status, at a Pearson r of 0.66 and p of 5×10^{-4} (Fig. 7D). ME6 shared 96 genes with the single-cell enterocyte DEGs, an 8.9% overlap representing 2.15-fold enrichment at hypergeometric $p < 0.001$ (Fig. 7E), and these genes peaked at day 4 in weaned piglets (Fig. 7F). Mfuzz clustering divided them into 6 temporal patterns, and the dominant pattern showed acute upregulation at day 4 followed by partial recovery at day 14 (Fig. 7G). This independent dataset therefore validates the single-cell findings and identifies day 4 as the key turning point (Fig. 7H).

Metagenomics reveals microbiota dysbiosis

To identify microbial drivers of enterocyte stress, we analyzed 24 fecal metagenomes with Kraken2 (PRJNA791695 [15]), 13 from the EWP/diarrhea group and 11 from the NSP/normal group. Alpha diversity did not differ between groups, with Shannon indices of 4.82 ± 0.31 in NSP and 4.65 ± 0.45 in EWP (Fig. 8A). Beta diversity told a different story. PCoA on Bray-Curtis distance showed partial separation, with PC1 explaining 28.4% and PC2 21.2% of variance and PERMANOVA giving R^2 of 0.18 at $p = 0.042$ (Fig. 8B). Potential pathogens were significantly enriched in EWP: *Desulfovibrio fairfieldensis* rose by a $\log_2$FC of 12.3 at $p = 0.001$, *Clostridium bornimense* by 11.8 at $p = 0.002$, and *Klebsiella pneumoniae* by 5.8 at $p = 0.015$. Butyrate producers moved the other way, with *Anaerostipes hadrus* down by 13.1 $\log_2$ units at $p = 0.001$ and *Parabacteroides* sp. CT06 down by 13.8 at $p = 0.001$ (Fig. 8C; Table S1). Two more butyrate producers, *Butyrivibrio* and *Roseburia*, showed consistent decreasing trends at

log_2FC of − 2.1 with p = 0.04 and − 1.8 with p = 0.06 (Fig. 8D). We integrated these layers into a multi-omics network that runs from microbiota dysbiosis through LPS/endotoxin increase and oxidative stress to EGR1/AREG-EGFR activation and enterocyte dysfunction (Fig. 8E–F).

Together these data tie microbiota dysbiosis to enterocyte dysfunction in a single association chain. Association, however, is not causation. Whether the AREG-EGFR axis functions as a molecular switch, or merely accompanies the stress response, can only be settled experimentally. We therefore turned to reductionist validation in IPEC-J2 cells.

Cell experiment validation

Six groups of IPEC-J2 cells were established and treated as described above. Relative to Control, TNF + IFN exposure significantly raised MT3, AREG, and CLDN4 mRNA levels (Fig. 9B). Western blotting showed the same trend at the protein level: EGFR phosphorylation intensified in the inflammation-mimicking group, MT3 and CLDN4 abundance rose, and gefitinib abolished EGFR phosphorylation while lowering repair protein expression (Fig. 9C). The inflammation-mimicking group also secreted more AREG and CCL20 into the medium, as measured by ELISA, which directly supports the autocrine hypothesis (Fig. 9D). Barrier assays told a consistent story. TEER fell and FITC-dextran permeability rose after inflammatory challenge; gefitinib aggravated both defects, whereas exogenous rAREG brought TEER back up and tightened paracellular permeability (Fig. 9E). In the rescue experiments, gefitinib-mediated EGFR blockade suppressed repair gene expression and damaged the barrier, and rAREG reversed each of these effects (Fig. 9F). The AREG-EGFR axis therefore behaves as the key molecular switch governing inflammation-induced epithelial barrier imbalance.

Discussion

Enterocyte remodeling and the three-dimensional stress phenotype

Weaning remains a major challenge in piglet production. By combining single-cell transcriptomics with temporal bulk RNA-seq and metagenomic data, we traced the multi-omics chain that links weaning stress to intestinal barrier breakdown. One cellular shift stood out in the atlas. Enterocytes accounted for only 2.4% of cells in NSP but expanded 2.4-fold to 5.8% in EWP, while proliferating/TA epithelial cells contracted. This points to compensatory accumulation of terminally differentiated cells rather than accelerated renewal. At the tissue level, the shift mirrors the villous atrophy and crypt deepening that Campbell et al. [1] documented after weaning, and it fits the finding of Boudry et al. [22] that arrested renewal of villous epithelium drives compensatory expansion of terminal enterocytes.

Such expansion erodes both the short-term and long-term functional integrity of intestinal absorption, secretion, and barrier properties. Enterocytes also carried by far the largest DEG burden of any epithelial subpopulation, at standard and strict thresholds alike. They are the primary effector cells of weaning

stress. Consistent with this picture, Smith et al. [23] showed that early weaning impairs mucosal barrier maturation in piglets, with intestinal permeability rising and tight junction structures altered.

The enterocyte DEGs were far from random. They assembled into a tightly coordinated three-dimensional pattern of "stress–repair–immune attenuation." Metallothionein MT3 topped the upregulated genes at a $\log_2$FC of 10.92, pointing to exceptionally severe oxidative stress; metallothioneins maintain redox homeostasis through zinc chelation and reactive oxygen species scavenging [24]. Within the scoring system, stress and repair scores correlated strongly and positively at r of 0.78. Enterocytes under intense oxidative pressure thus appear to launch a functional reprogramming that shifts limited resources away from immune surveillance toward antioxidant defense and barrier repair. This pattern offers a quantitative phenotypic frame for reading enterocyte biology under weaning stress. Tight junction proteins, including claudins, occludin, and ZO-1, are dynamically regulated in the weaned piglet intestine, and their disruption leads directly to barrier dysfunction [25]. Our data fit the same frame but with a twist: CLDN4 transcripts rose, yet barrier function did not recover. We call this scenario "transcriptional compensation but functional non-recovery."

At the strict threshold, the 174 core upregulated genes enriched 110 GO BP terms (Figure S7), more than the 51 terms at the standard threshold (Fig. 2G). The paradox has a simple explanation. Strongly differential genes concentrate in energy metabolism and stress response, while numerous weakly differential genes introduce noise that dilutes enrichment significance. Downregulated genes behaved oppositely, enriching only 2 GO terms at the strict threshold (Figure S7). Their high functional heterogeneity likely reflects simultaneous silencing of multiple immune and metabolic pathways.

Integration of autocrine signaling, differentiation trajectory, and transcriptional regulation

The three-dimensional pattern implies a fundamental reprogramming of enterocyte priorities. What drives the repair arm upstream? The significant immune infiltration made paracrine inflammatory signals an obvious candidate. NicheNet analysis argued otherwise: the predicted regulatory potential of AREG for repair target genes far exceeded that of other immune ligands, and CellChat confirmed a 38% increase in AREG-EGFR communication strength in EWP. Despite significant immune infiltration, the enterocyte repair program is driven primarily by self-produced AREG rather than paracrine signals from immune cells. Zaiss et al. [7] reported in an inflammatory bowel disease model that epithelium-derived AREG contributes more to barrier repair than immune-derived AREG. Our study validates the universality of this rule in a weaning stress model and suggests that enterocytes possess significant repair autonomy in the stress microenvironment.

The timing of autocrine signaling is therefore a question of central interest. On the Slingshot trajectory, EWP cells already expressed stress-repair genes such as MT3, AREG, and CLDN4 at high levels at the TA stage and held them through terminal differentiation. In NSP, the same genes crested only in terminal enterocytes. Proliferation markers waned earlier in EWP, and the immune gene SFTPD stayed

suppressed throughout. This "premature activation" indicates that weaning stress disrupts normal epithelial differentiation timing. Cells are forced to undertake repair functions before full maturation, which can lead to differentiation program disorder and barrier insufficiency.

Hu et al. [3] reported that after weaning, villous epithelial renewal is arrested and immature cells differentiate prematurely; villous height then decreases, and the reduced absorption area leads to villous atrophy. Miyoshi et al. [26] demonstrated that endoplasmic reticulum stress causes rapid loss of intestinal epithelial stemness and accelerates directed differentiation of transit-amplifying cells. EWP cells in our data showed exactly this signature: lower median pseudotime and premature activation of repair genes. A similar stress-induced disorder of the stem cell–progenitor–mature cell axis therefore seems to operate during weaning.

Premature activation of the repair program implies an upstream molecular switch triggered at early differentiation stages. Among the TF candidates, the extreme upregulation of EGR1 at $p < 2.2\times10^{-16}$ makes it the prime suspect. As an immediate early response factor, EGR1 is rapidly induced by oxidative stress and inflammatory stimuli and binds GC-rich promoter elements to regulate downstream targets [21]. Here, EGR1 correlated positively with every target examined, and AREG sat at the core of the regulatory network. Together the evidence supports an EGR1–AREG-EGFR–repair regulatory axis. EGR1 may thus act as the early molecular switch of weaning stress, converting upstream stress signals into downstream repair programs.

Cross-platform temporal validation and microbiota tracing

Single-cell data provide high-resolution snapshots but cannot capture temporal dynamics after weaning. The PRJEB54752 temporal dataset supplied the complementary evidence. WGCNA independently identified module ME6 as strongly associated with weaning status at r of 0.66, sharing 96 genes with single-cell enterocyte DEGs at hypergeometric $p < 0.001$. The enterocyte stress response is therefore a genuine biological signal that reproduces across platforms and time scales, not an artifact of single-cell analysis. In Mfuzz clustering these genes crested at day 4 and had only partly recovered by day 14, marking day 4 as the acute turning point of weaning. Clinically, PWD incidence likewise peaks 3–5 days after weaning [27].

Temporal validation alone cannot explain the complete weaning mechanism; the upstream drivers of the chain still need elucidation. Metagenomics showed that *Desulfovibrio*, *Clostridium*, and other potential pathogens were significantly enriched in EWP, while *Anaerostipes*, *Parabacteroides*, and other butyrate producers were severely depleted. Butyrate is a key metabolite of colonic microbiota. Beyond serving as the primary energy source for colonic epithelium, it influences small intestinal barrier function through systemic GPR43 signaling and HDAC inhibition [2, 11]. Zheng et al. [11] reported that microbiota-derived butyrate enhances barrier function by suppressing claudin-2 through an IL-10 receptor-dependent pathway.

Depletion of butyrate producers can therefore trigger a cascade. Weakened systemic SCFA signaling and a compromised colonic barrier promote LPS translocation [28]. LPS then activates EGR1 in ileal enterocytes through the TLR4-NFκB pathway [29], and EGR1 transcriptionally regulates downstream chemokines including CCL20 [30]. Tight junction proteins are upregulated at the transcriptional level in an attempt to reinforce the barrier, but their function may be impaired by energy deficiency and oxidative damage [31]. These mechanisms integrate microbiota dysbiosis with epithelial dysfunction and complete a "butyrate deficiency–oxidative stress–EGR1–AREG-EGFR" chain from environmental stress to cellular injury.

Hierarchical causal inference and molecular switch establishment

Multi-omics correlation builds a relatively complete mechanistic chain, but correlation is not causation. In bulk and single-cell transcriptomes alike, correlation analysis captures population-level covariation. It cannot distinguish whether AREG-EGFR activation drives barrier repair or simply accompanies inflammation. The EGR1-AREG correlation in EWP enterocytes may reflect direct transcriptional regulation, or both factors may be driven by shared upstream inflammatory signals. The metagenomic evidence carries its own caveat: the link between butyrate depletion and barrier dysfunction remains correlational, and fecal communities are at best a proxy for the ileal luminal microbiota that actually contact enterocytes. Closing this causal gap required a reductionist system. We chose IPEC-J2 cells, a porcine small intestinal epithelial line that preserves the species-specific signaling architecture of primary ileal enterocytes [32].

To reproduce the weaning inflammatory milieu, we combined TNF-α with IFN-γ, two cytokines that typify early intestinal stress after weaning and converge on EGR1 induction through the NF-κB and STAT1 pathways [3]. Readouts at three levels, qPCR for transcription, Western blot for translation, and ELISA for secretion, gave convergent evidence that treated cells recapitulate the molecular signature of in vivo EWP enterocytes, with MT3, AREG, and CLDN4 all elevated. TEER and FITC-dextran permeability then tied these molecular changes directly to barrier physiology, following established IPEC-J2 monolayer protocols [32].

Causality was tested bidirectionally. Gefitinib, a selective EGFR tyrosine kinase inhibitor, silenced endogenous AREG signaling; rAREG was added back to restore it. Gefitinib eliminated the repair response and worsened barrier dysfunction, establishing necessity. rAREG brought TEER back up and permeability back down even under sustained inflammatory injury, establishing sufficiency. Moving from multi-omics correlation to cellular causation, we position the AREG-EGFR axis as the molecular switch governing weaning stress-induced intestinal epithelial barrier imbalance, and as an actionable entry point for precise nutritional intervention against PWD.

This study integrates multi-omics data to demonstrate how weaning stress unbalances the intestinal barrier. Microbiota dysbiosis and immune infiltration activate EGR1 and the AREG-EGFR autocrine repair program in enterocytes. Innate immune attenuation and differentiation trajectory disorder accompany

these changes, and the barrier ultimately fails. The "stress–repair–immune attenuation" three-dimensional pattern of enterocytes is the core cellular mechanism of PWD, and the AREG-EGFR axis together with butyrate supplementation represents a potential intervention target.

Conclusions

Weaning stress drives a three-dimensional reprogramming of ileal enterocytes, combining coordinated oxidative stress, autocrine repair activation, and innate immune attenuation, through an EGR1–AREG–EGFR signaling axis. The result is intestinal barrier dysfunction in early-weaned piglets. Multi-omics integration connects this epithelial program to gut microbiota dysbiosis and butyrate-producer depletion. Cell-based blockade and rescue experiments confirm AREG–EGFR signaling as a causal switch for barrier imbalance. The EGR1–AREG–EGFR axis and butyrate supplementation therefore represent candidate targets for mitigating weaning-induced intestinal barrier injury in piglets.

Abbreviations

AREG
amphiregulin
BH
Benjamini-Hochberg
bulk RNA-seq
bulk RNA sequencing
CLR
centered log-ratio
DEG
differentially expressed gene
EGFR
epidermal growth factor receptor
EWP
early-weaned piglet
FC
fold change
GO
Gene Ontology
KEGG
Kyoto Encyclopedia of Genes and Genomes
LPS
lipopolysaccharide
ME
module eigengene
NSP

normal suckling piglet
PCoA
principal coordinate analysis
PERMANOVA
permutational multivariate analysis of variance
PWD
post-weaning diarrhea
qPCR
quantitative polymerase chain reaction
ROS
reactive oxygen species
scRNA-seq
single-cell RNA sequencing
SCFA
short-chain fatty acid
TA
transit-amplifying
TEER
transepithelial electrical resistance
TNF-α
tumor necrosis factor-alpha
UMAP
uniform manifold approximation and projection
WGCNA
weighted gene co-expression network analysis.

Declarations

Ethics approval and consent to participate

The animal procedures in the original studies from which the public datasets were derived were approved by the respective institutional ethics committees of the original investigators: the bulk RNA-seq study (PRJEB54752) was approved by the University of Nottingham Animal Welfare and Ethical Review Body (AWERB), and the single-cell study (GSE174112) was approved by the Animal Care and Use Committee of Zhejiang University (Ethics Code Permit ZJU20170529). The in vitro portion of this study did not involve live animal procedures; IPEC-J2 is an established cell line (ATCC CRL-183) and does not require additional animal ethics approval.

Consent for publication

Not applicable.

Availability of data and materials

The single-cell RNA sequencing datasets analyzed during the current study are available in the Gene Expression Omnibus repository (GSE174112; https://www.ncbi.nlm.nih.gov/geo/query/acc.cgi?acc=GSE174112) [33]. The bulk RNA-seq datasets analyzed during the current study are available in the European Nucleotide Archive repository (PRJEB54752; https://www.ebi.ac.uk/ena/browser/view/PRJEB54752) [14]. The metagenomic datasets analyzed during the current study are available in the NCBI Sequence Read Archive repository (PRJNA791695; https://www.ncbi.nlm.nih.gov/sra/PRJNA791695) [15]. The Sus scrofa reference genome Sscrofa11.1 (Ensembl release 100) is available at http://www.ensembl.org. All source code and analysis pipelines are available from the corresponding author upon reasonable request.

Competing interests

The authors declare that they have no competing interests.

Funding

This study was funded by the Fundamental Research Program of Shanxi Province (Grant No. 202403021212081), the Doctoral Graduates and Postdoctoral Researchers from Shanxi Province Come to Work to Reward Scientific Research Projects (No. SXBYKY2024030), the Doctoral Research Starting Project at Shanxi Agricultural University (No. 2023BQ59), and the Shanxi Scholarship Council of China (No. 2025-120). The funding bodies played no role in the design of the study; in the collection, analysis, and interpretation of data; or in the writing of the manuscript.

Authors' contributions

YH: conceptualization, methodology, investigation, writing - original draft, funding acquisition. DQ: data curation, formal analysis, visualization. PL: validation, investigation. WY: resources, formal analysis. RH: supervision, project administration, writing - review & editing, funding acquisition. All authors read and approved the final manuscript.

Acknowledgements

The authors thank Shanxi Agricultural University and the Hospital of Stomatology, Shanxi Medical University, for providing research facilities and technical support. The mechanism diagrams in this manuscript (Figure 8F and Figure 9A) were created with the AI tool PicDoc; the authors reviewed and edited all AI-generated content and take full responsibility for its accuracy and integrity.

References

1. Campbell JM, Crenshaw JD, Polo J. The biological stress of early weaned piglets. J Anim Sci Biotechnol. 2013;4:19.

2. Gresse R, Chaucheyras-Durand F, Fleury MA, et al. Gut microbiota dysbiosis in post-weaning piglets: understanding the keys to health. Trends Microbiol. 2017;25:851–73.
3. Hu CH, Xiao K, Luan ZS, Song J. Early weaning increases intestinal permeability, alters expression of cytokine and tight junction proteins, and activates mitogen-activated protein kinases in pigs. J Anim Sci. 2013;91:1094–101.
4. Tang W, Zhong Y, Wei Y, et al. Ileum tissue single-cell mRNA sequencing elucidates the cellular architecture of pathophysiological changes associated with weaning in piglets. BMC Biol. 2022;20:123.
5. Wiarda JE, Trachsel JM, Sivasankaran SK, Tuggle CK, Loving CL. Intestinal single-cell atlas reveals novel lymphocytes in pigs with similarities to human cells. Life Sci Alliance. 2022;5:e202201442.
6. Wong VW, Stange EF, Hegazy AN, et al. Epidermal growth factor receptor (EGFR) signaling regulates intestinal epithelial cell proliferation and migration during mucosal healing. Inflamm Bowel Dis. 2012;18:2393–402.
7. Zaiss DMW, Gause WC, Osborne LC, Artis D. Emerging functions of amphiregulin in orchestrating immunity, inflammation, and tissue repair. Immunity. 2015;42:216–26.
8. Guevarra RB, Lee JH, Lee SH, Seok MJ, Kim DW, Kang BN, et al. Piglet gut microbial shifts early in life: causes and effects. J Anim Sci Biotechnol. 2019;10:1.
9. Wang HB, Wang PY, Wang X, Wan YL, Liu YC. Butyrate enhances intestinal epithelial barrier function via up-regulation of tight junction protein Claudin-1 transcription. Dig Dis Sci. 2012;57:3126–35.
10. Liu H, Zhao J, Zhang W, Nie C. Impacts of sodium butyrate on intestinal mucosal barrier and intestinal microbial community in a weaned piglet model. Front Microbiol. 2022;13:1041885.
11. Zheng L, Kelly CJ, Battista KD, et al. Microbial-derived butyrate promotes epithelial barrier function through IL-10 receptor-dependent repression of claudin-2. J Immunol. 2017;199:2976–84.
12. Korsunsky I, Millard N, Fan J, et al. Fast, sensitive and accurate integration of single-cell data with Harmony. Nat Methods. 2019;16:1289–96.
13. Hao Y, Hao S, Andersen-Nissen E, et al. Integrated analysis of multimodal single-cell data. Cell. 2021;184:3573–87.
14. Le Bon M, Tötemeyer S, Emes RD, Mellits KH. Gut transcriptome reveals differential gene expression and enriched pathways linked to immune activation in response to weaning in pigs. PRJEB54752. Eur Nucleotide Archive. 2022.
15. Zhou X, Liu Y, Xiong X, Chen J, Tang W, He L, et al. Intestinal accumulation of microbiota-produced succinate caused by loss of microRNAs leads to diarrhea in weanling piglets. PRJNA791695. NCBI Sequence Read Archive; 2022.
16. Browaeys R, Saelens W, Saeys Y. NicheNet: modeling intercellular communication by linking ligands to target genes. Nat Methods. 2020;17:159–62.
17. Jin S, Guerrero-Juarez CF, Zhang L, et al. Inference and analysis of cell-cell communication using CellChat. Nat Commun. 2021;12:1088.

18. Street K, Risso D, Fletcher RB, et al. Slingshot: cell lineage and pseudotime inference for single-cell transcriptomics. BMC Genomics. 2018;19:477.
19. Langfelder P, Horvath S. WGCNA: an R package for weighted correlation network analysis. BMC Bioinformatics. 2008;9:559.
20. Kumar L, Futschik ME. Mfuzz: a software package for soft clustering of microarray data. Bioinformation. 2007;2:5–7.
21. Thiel G, Cibelli G. Regulation of life and death by the zinc finger transcription factor Egr-1. J Cell Physiol. 2002;193:287–92.
22. Boudry G, Péron V, Le Huérou-Luron I, Lallès JP, Sève B. Weaning induces both transient and long-lasting modifications of absorptive, secretory, and barrier properties of piglet intestine. J Nutr. 2004;134:2256–62.
23. Smith F, Clark JE, Overman BL, et al. Early weaning stress impairs development of mucosal barrier function in the porcine intestine. Am J Physiol Gastrointest Liver Physiol. 2010;298:G352–63.
24. Thirumoorthy K, Manisenthil Kumar KT, Shyam Sundar A, et al. Metallothionein: an overview. World J Gastroenterol. 2007;13:993–6.
25. Wang J, Ji H. Tight junction proteins in the weaned piglet intestine: roles and regulation. Curr Protein Pept Sci. 2019;20:652–60.
26. Miyoshi H, Ajima R, Luo CT, et al. ER stress causes rapid loss of intestinal epithelial stemness through activation of the unfolded protein response. Cell Rep. 2013;3:1858–62.
27. Heo JM, Opapeju FO, Pluske JR, Kim JC, Hampson DJ, Nyachoti CM. Gastrointestinal health and function in weaned pigs: a review of feeding strategies to control post-weaning diarrhoea without using in-feed antimicrobial compounds. J Anim Physiol Anim Nutr. 2013;97:207–37.
28. Cani PD, Amar J, Iglesias MA, et al. Metabolic endotoxemia initiates obesity and insulin resistance. Diabetes. 2007;56:1761–72.
29. Yao J, Mackman N, Edgington TS, Fan ST. Lipopolysaccharide induction of the tumor necrosis factor-alpha promoter in human monocytic cells. Regulation by Egr-1, c-Jun, and NF-kappaB transcription factors. J Biol Chem. 1997;272:17795–801.
30. Hoffmann E, Dittrich-Breiholz O, Holtmann H, Kracht M. Transcriptional regulation of EGR-1 by the interleukin-1-JNK-MKK7-c-Jun pathway. J Biol Chem. 2008;283:13389–98.
31. Rao R. Oxidative stress-induced disruption of epithelial and endothelial tight junctions. Front Biosci. 2008;13:7210–26.
32. Wu J, He C, Bu J, et al. Betaine attenuates LPS-induced downregulation of Occludin and Claudin-1 and restores intestinal barrier function. BMC Vet Res. 2020;16:75.
33. Tang W, Zhong Y, Wei Y et al. Ileum tissue single-cell mRNA sequencing elucidates the cellular architecture of pathophysiological changes associated with weaning in piglets. GSE174112. Gene Expression Omnibus. 2022.

Figures

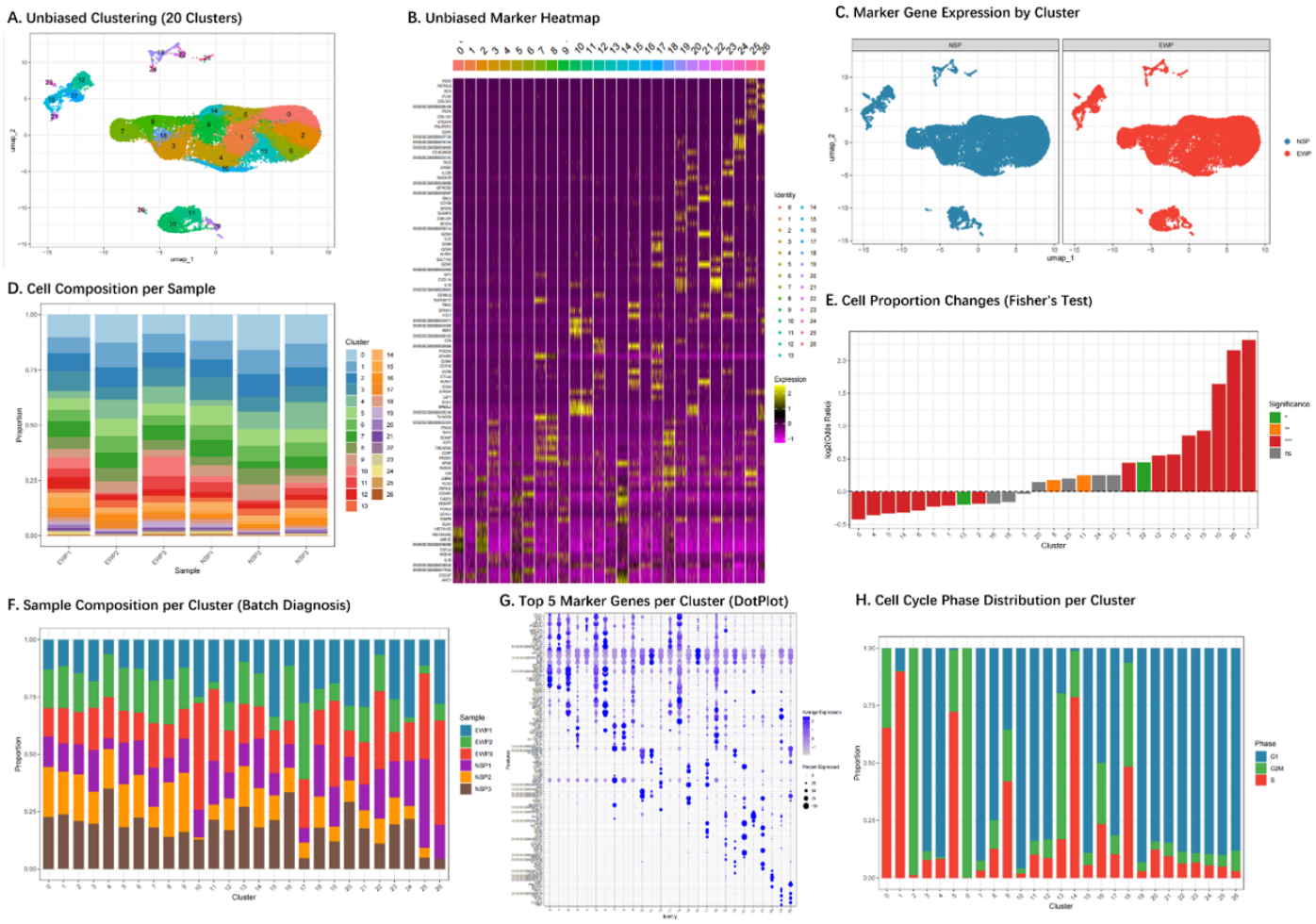


Figure 1

Weaning stress reshapes ileal cellular composition in piglets. (A) UMAP unbiased clustering of 45,258 cells after Harmony correction (25 clusters, derived from initial 27 clusters). (B) Representative marker gene expression heatmap for each cluster. (C) UMAP distribution of NSP and EWP cells. (D) Stacked bar plot of 14 cell-type proportions. (E) Comparison of enterocyte proportions between groups (Fisher's exact test, EWP 5.8% vs. NSP 2.4%). (F) Statistical tests of proportion changes for each cell type (Fisher's exact test, red indicates significance). (G) Per-cluster sample-source stacked plot (batch diagnosis). (H) Top 5 marker gene DotPlot (cell-type annotation validation). (I) Cell-cycle phase distribution per cluster (proliferation-state validation).

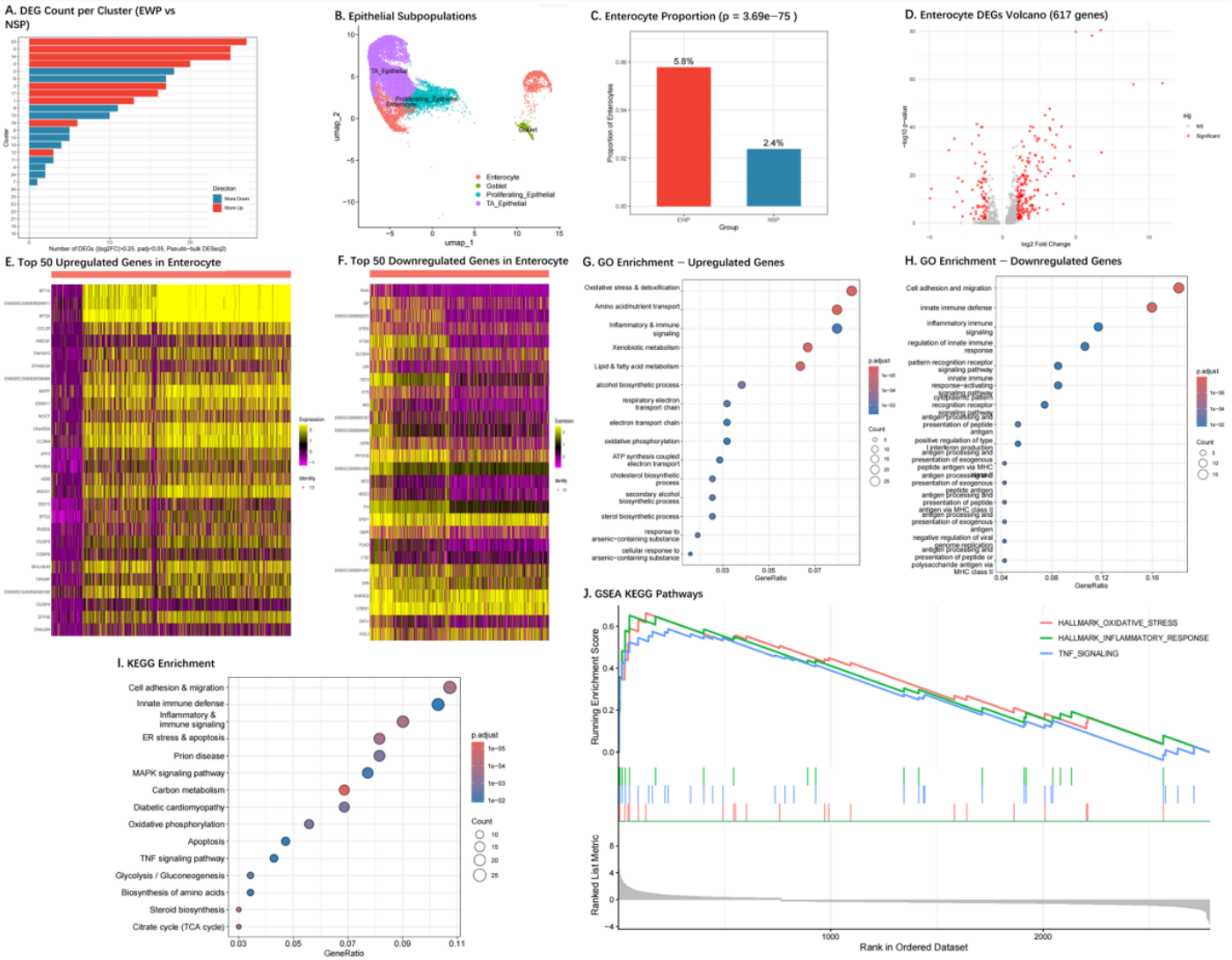


Figure 2

Enterocytes are the core responder cells to weaning stress. (A) DEG counts ranked across 27 clusters (Wilcoxon test). (B) Enterocyte subcluster UMAP (cluster 10 absorptive and cluster 20 secretory). (C) Enterocyte proportion bar plot (NSP vs. EWP). (D) Volcano plot of 617 enterocyte DEGs (472 up, 145 down, Wilcoxon, $|\log_2 FC| > 0.25$). (E) Top 50 upregulated gene heatmap. (F) Top 50 downregulated gene heatmap. (G) GO BP enrichment of upregulated genes (51 significant terms, standard threshold). (H) GO BP enrichment of downregulated genes (27 significant terms, standard threshold). (I) KEGG pathway enrichment (20 significant pathways, standard threshold). (J) GSEA KEGG pathway enrichment (41 significant pathways).

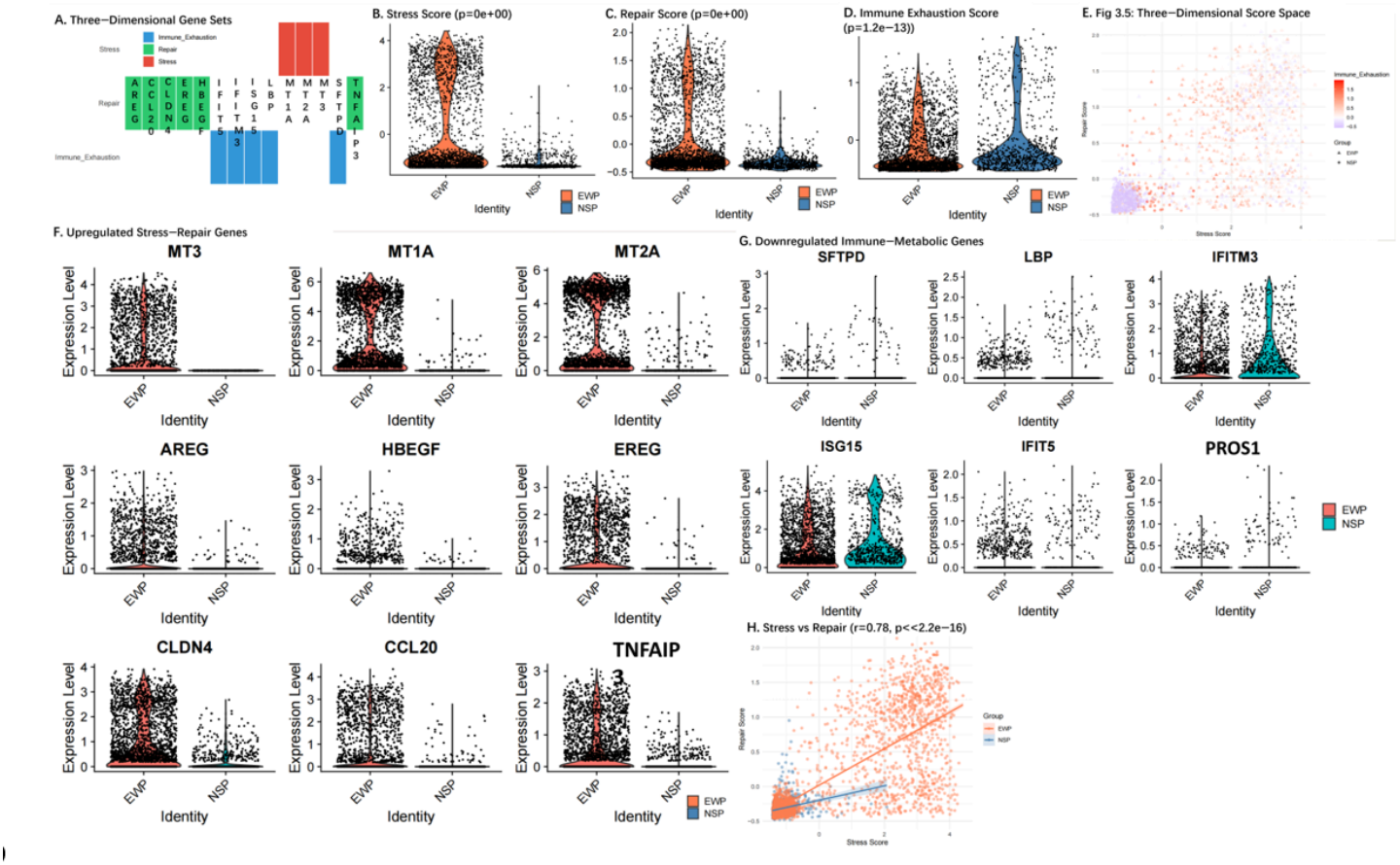


Figure 3

The "stress–repair–immune attenuation" three-dimensional pattern of enterocytes. (A) Definitions of the three-dimensional scoring gene sets. (B) Stress score violin plot (NSP mean −1.22 vs. EWP 0.31). (C) Repair score violin plot (NSP −0.32 vs. EWP 0.10). (D) Immune attenuation score violin plot (NSP 0 vs. EWP −0.14). (E) Three-dimensional scatter plot. (F) Core upregulated gene expression violin plots. (G) Core downregulated gene expression violin plots. (H) Correlation between stress and repair scores (Pearson r = 0.78, $p < 2.2\times10^{-16}$), indicating coordinated activation of antioxidant and barrier repair programs.

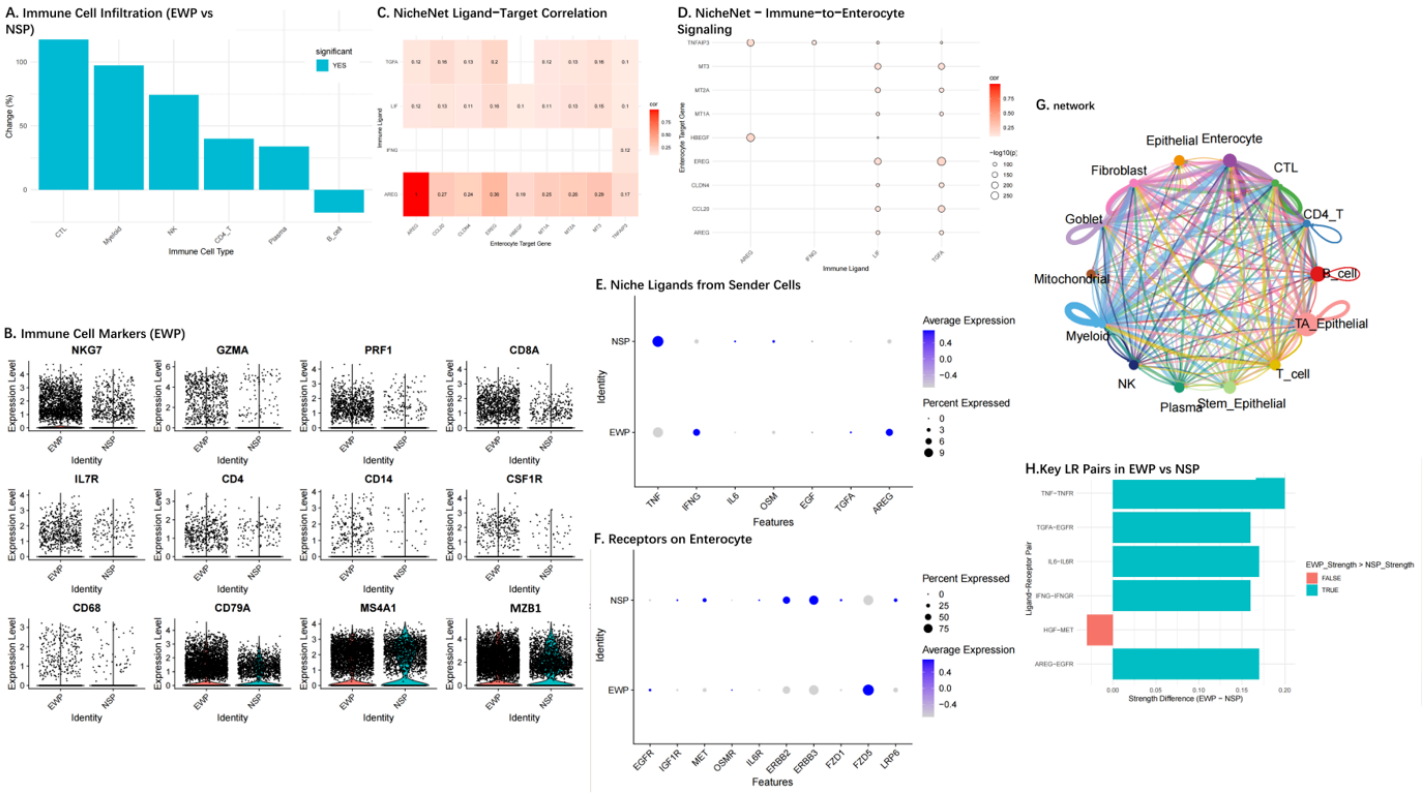


Figure 4

Immune-enterocyte interaction network. (A) Summary of immune cell proportion changes. (B) Immune cell marker expression. (C) NicheNet ligand–target gene correlation matrix (27 significant pairs). (D) NicheNet significant correlation bubble plot. (E) Sender-cell ligand DotPlot (IL1B not detected, possibly due to dissociation-induced myeloid cell loss or rapid mRNA degradation). (F) Enterocyte receptor DotPlot (all 10 receptors available). (G) CellChat total communication network (NSP). (H) Key ligand–receptor pair statistics in EWP vs. NSP (AREG-EGFR +38%).

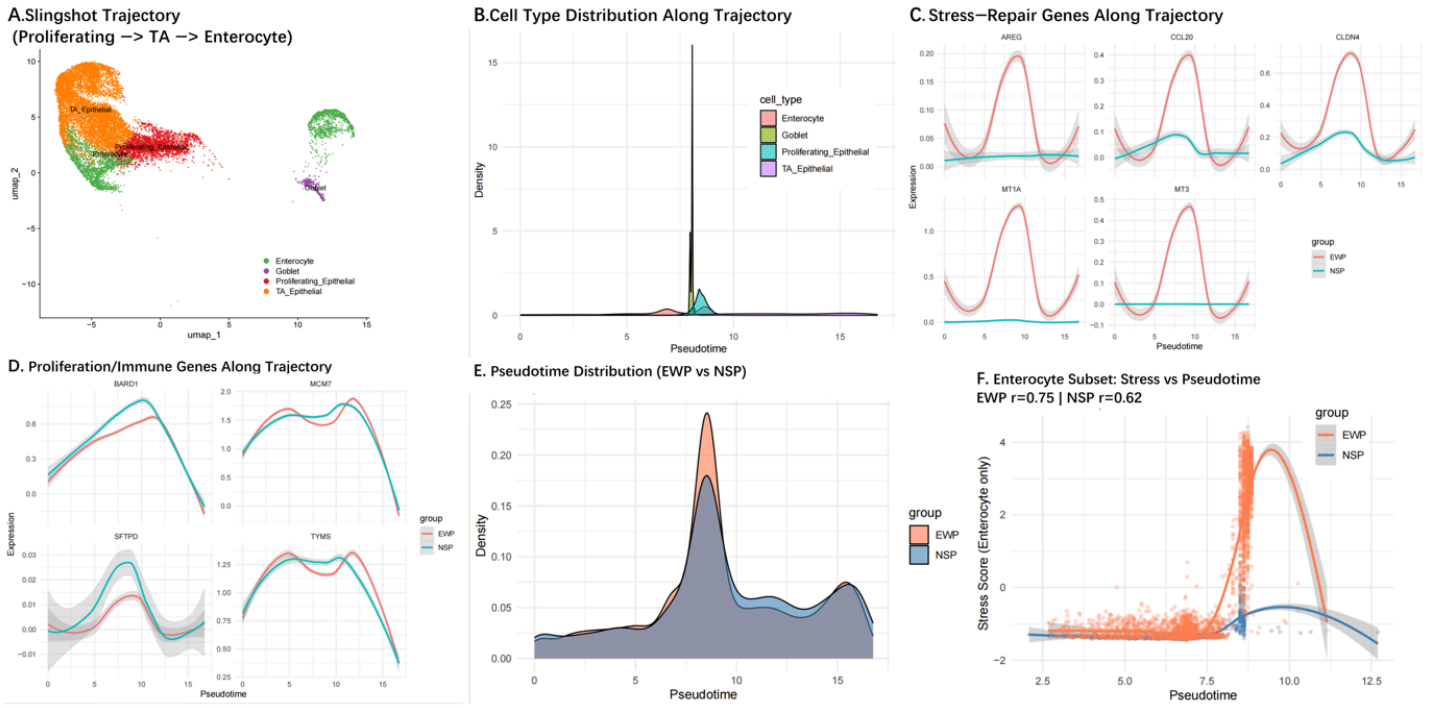


Figure 5

Gene dynamics along the epithelial differentiation trajectory. (A) Slingshot pseudotime trajectory (16,190 cells, 2 lineages, starting from Proliferating_Epithelial). (B) Cell-type distribution density along the trajectory. (C) Stress-repair gene dynamics along the trajectory (loess smoothing). (D) Proliferation/immune gene dynamics along the trajectory. (E) Pseudotime distribution between groups (KS D = 0.068, p = 3×10^{-14}). (F) Stress score changes along the trajectory in the enterocyte subset (EWP r = 0.75, NSP r = 0.62).

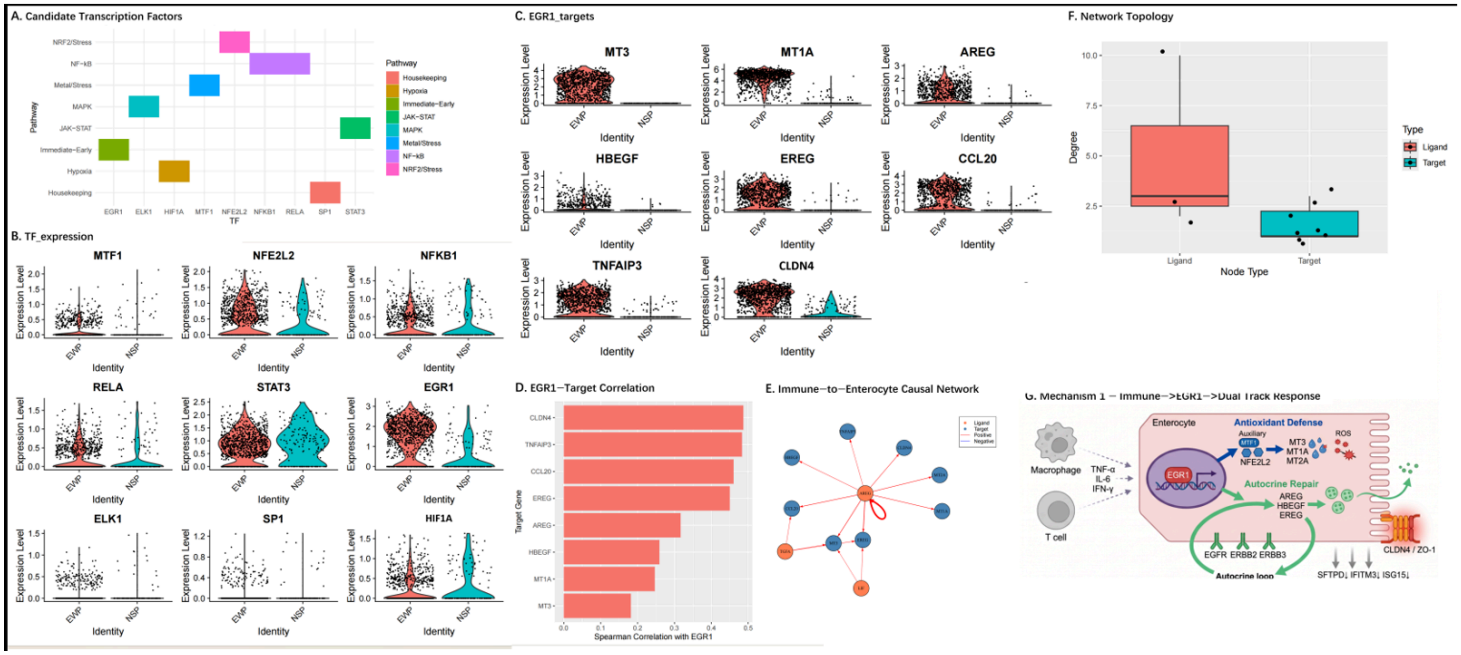


Figure 6

Transcriptional regulation and regulatory network. (A) Candidate transcription factor screening. (B) Transcription factor expression violin plots. (C) Expression of predicted EGR1 target genes. (D) Spearman correlation bar plot between EGR1 and target genes. (E) Immune-enterocyte regulatory network (igraph). (F) Network topology analysis (degree centrality). (G) Mechanism diagram: immune infiltration → EGR1 activation → dual-track response (antioxidant defense plus autocrine repair).

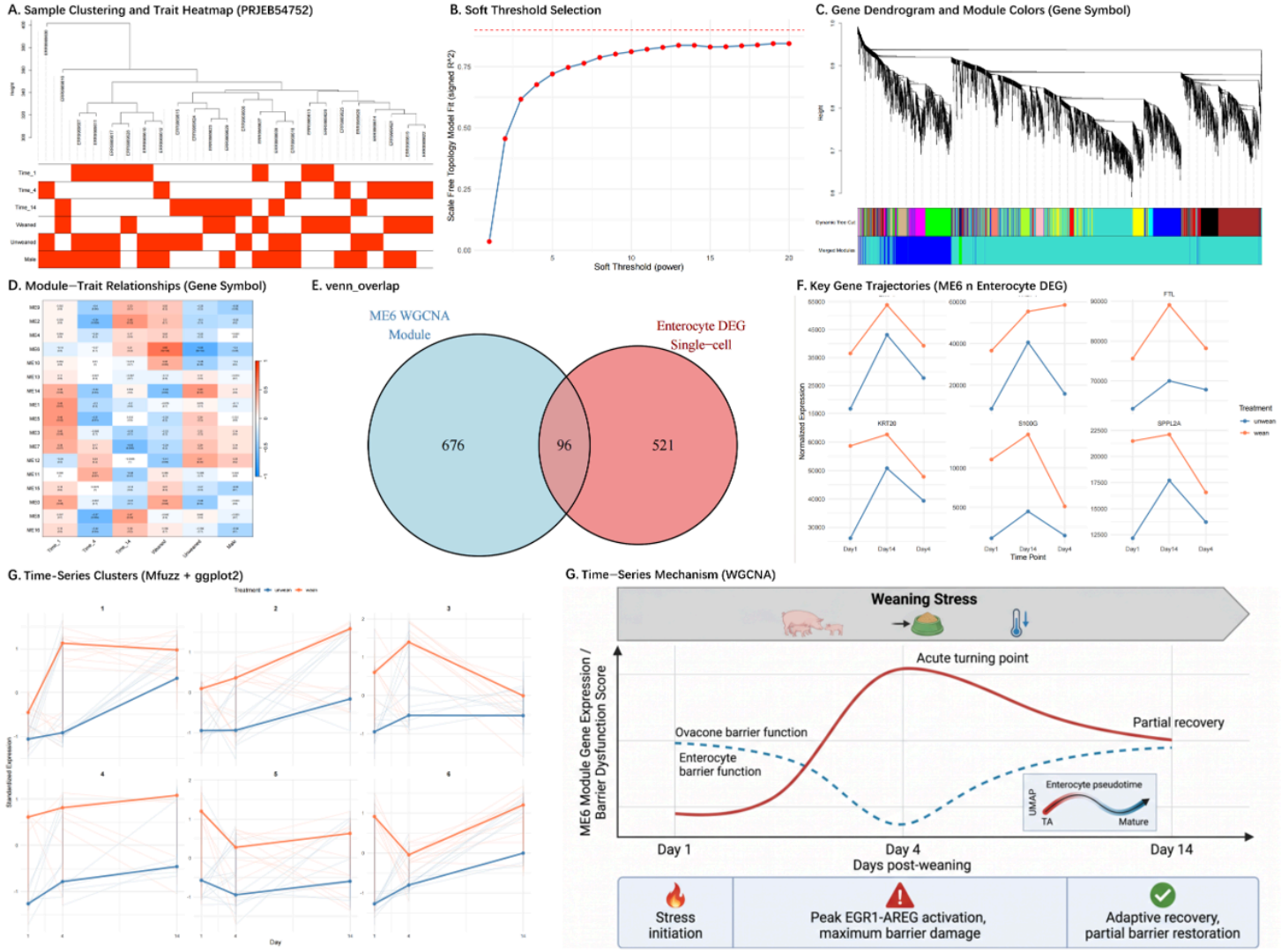


Figure 7

WGCNA temporal validation. (A) Sample clustering tree and trait heatmap. (B) Soft-thresholding selection (scale-free topology). (C) Gene clustering tree and module colors. (D) Module–trait association heatmap. (E) Venn diagram of ME6 and enterocyte DEG overlap. (F) Temporal trajectories of key genes. (G) Mfuzz temporal clustering. (H) Time-series mechanism schematic.

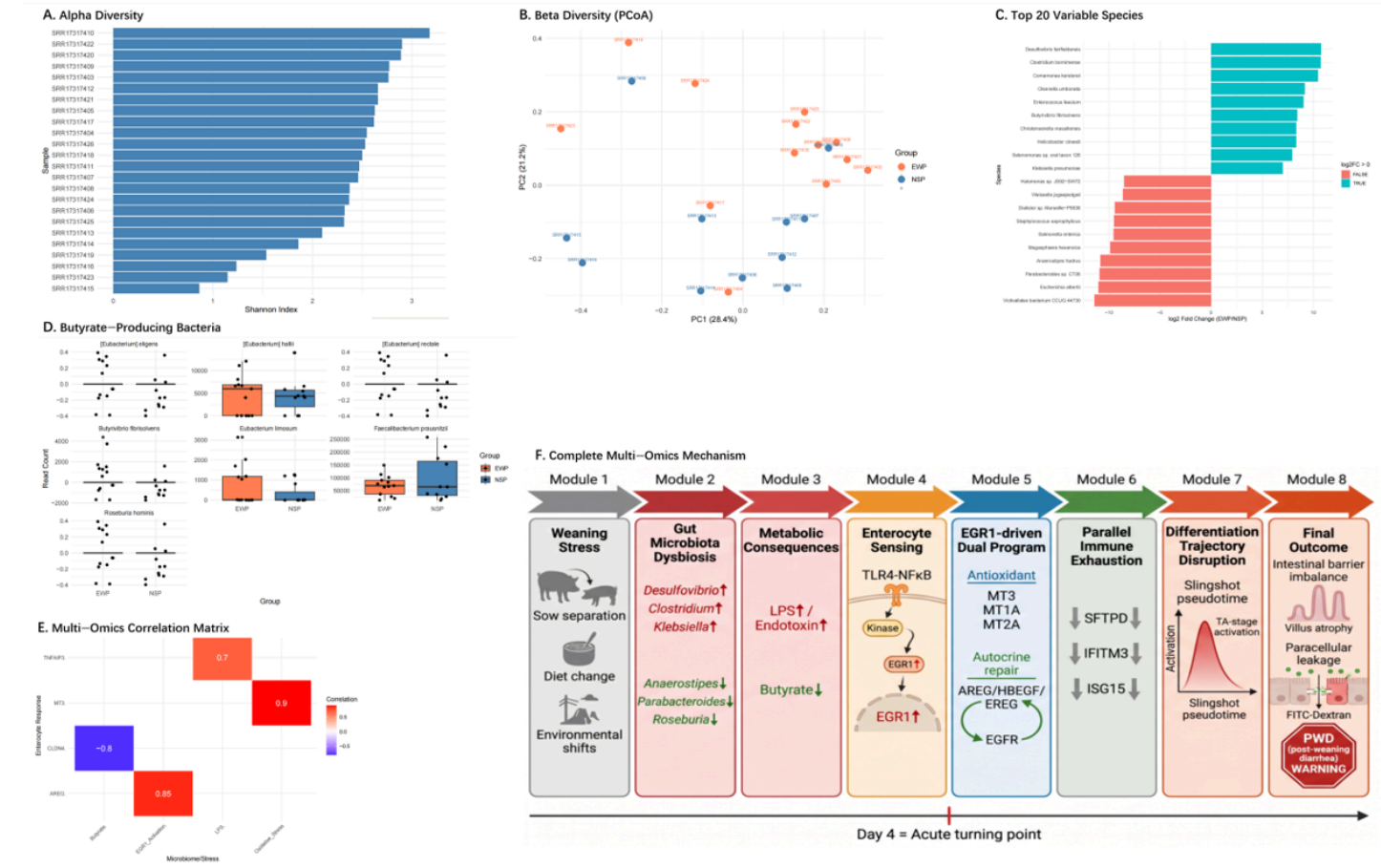


Figure 8

Metagenomics and multi-omics integration. (A) Alpha diversity (Shannon index). (B) Beta diversity PCoA (Bray-Curtis). (C) Top 20 differential species (Wilcoxon test, BH correction). (D) Abundance of butyrate-producing bacteria. (E) Correlation heatmap. (F) Diagram of the complete mechanism.

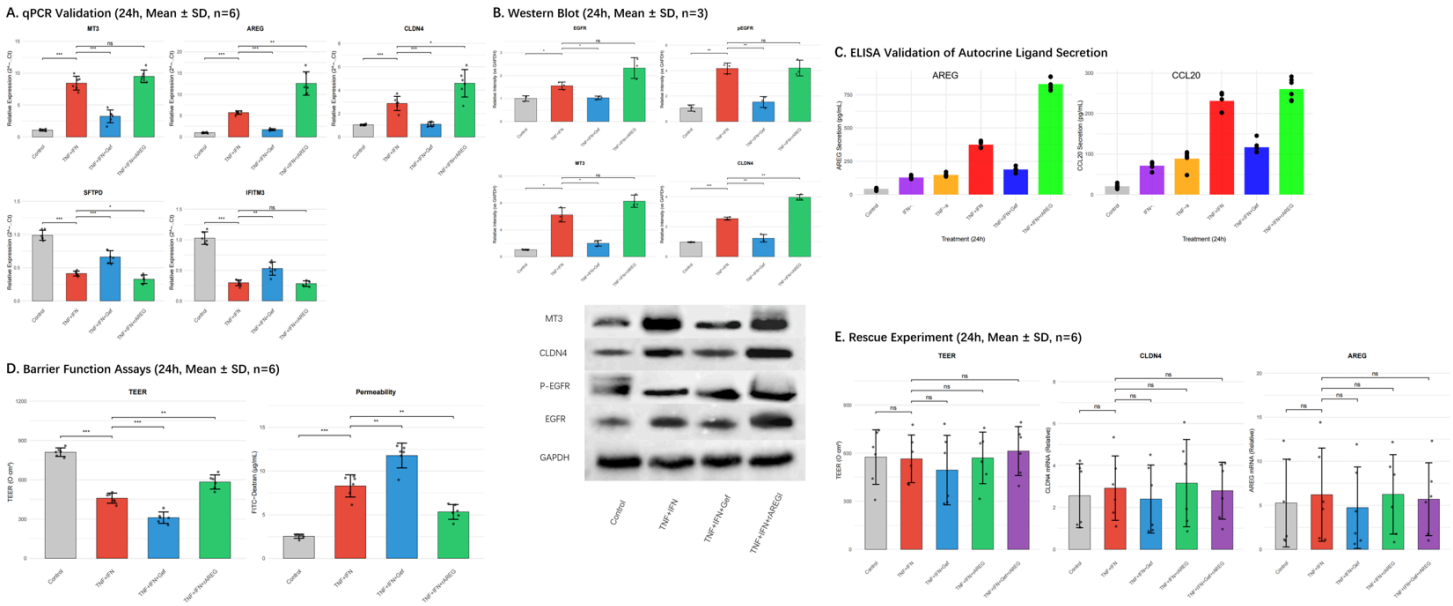


Figure 9

Validation of the AREG-EGFR axis in cultured cells. (A) Schematic of the IPEC-J2 experimental design (6 groups, n = 6). (B–F) Results from three independent experiments: (B) qPCR analysis of key gene expression ($2^{-}\Delta\Delta Ct$); (C) Western blot analysis of EGFR, p-EGFR, MT3, and CLDN4 protein levels; (D) ELISA quantification of AREG and CCL20 secreted into the culture medium, directly testing the autocrine hypothesis; (E) TEER and FITC-dextran permeability measurements of barrier function; (F) rescue experiment testing the causal effects of gefitinib-mediated EGFR blockade and rAREG supplementation.

Supplementary Files

This is a list of supplementary files associated with this preprint. Click to download.

- supplementaryfile.pdf